

Tunable crystallographic grain orientation and Raman fingerprints of polycrystalline SnO thin films†

Quan Liu,^{ab} Lingyan Liang,^{*a} Hongtao Cao,^{*a} Hao Luo,^a Hongliang Zhang,^a Jun Li,^a Xiuxia Li^a and Fuling Deng^a

In this study, (001) and (101)-orientated polycrystalline SnO films were respectively fabricated. The preferred orientation conversion was observed by modifying the stoichiometry of the SnO films. It was revealed that the O-rich and Sn-rich SnO films favor (001) and (101) grain orientations, respectively. Moreover, based on the Raman selection rule and our experimental results, the 110 cm⁻¹ Raman peak is assigned to the low-frequency E_g mode of SnO. The Raman intensity ratio between the 110 cm⁻¹ and 210 cm⁻¹ peak of SnO increases with the relative texture coefficient of the (101) grain orientation but decreases with that of the (001) one, demonstrating that the Raman characteristic information could be used as fingerprint recognition to mutually predict the crystallographic texture of SnO films.

Introduction

Tin monoxide (SnO), a simple binary oxide, has attracted increasing attention due to its numerous applications in thin-film transistors (TFTs), lithium rechargeable batteries,^{1,2} gas sensors,³ and so on. In particular, both p-type and ambipolar TFTs have been demonstrated by using SnO channels.⁴⁻⁹ The maximum field-effect mobility of p-type SnO TFTs has exceeded 10 cm² V⁻¹ s⁻¹ so far,⁸ and the gain of the CMOS-like inverter based on ambipolar SnO TFTs is up to 30.⁹

SnO is known to have a tetragonal litharge-type (*P4/nmm*) crystallographic structure. This structure is characteristic of anisotropy because SnO is layered in the [001] crystallographic direction with a van der Waals gap of 2.52 Å in-between two adjacent Sn planes.¹⁰ Thus, the electrical and optical properties of the layered-structure SnO are expected to be anisotropic due to its structural anisotropy. For example, it was predicted by theoretical calculation that the hole effective mass of SnO is anisotropic and hole carriers may hop more easily in the interlayer than in the intralayer region.¹¹ Until now, the preferred (001)-orientated SnO films can be prepared on single crystal substrates such as γ-plane sapphire,¹² (001) rock salt,¹³ or (001) yttria-stabilized zirconia.¹⁴ However, SnO films with other preferred orientations are rarely reported.

It has been reported that Raman spectra of SnO thin films showed two peaks located around 110 and 210 cm⁻¹, respectively. The peak at 210 cm⁻¹ was assigned to A_{1g} mode definitely, in line with the theoretical calculations and experimental reports.¹⁵⁻¹⁹ However, there is a considerable controversy on the identification of the peak at 110 cm⁻¹, which is allocated to either B_{1g} or the low-frequency E_g mode. Some researchers considered that the peak centered at 110 cm⁻¹ was designated as B_{1g} mode based on their experiments.^{15,16} But nevertheless, according to the theoretical calculations, the phonon frequency of low-frequency E_g mode ranges from 113 to 143 cm⁻¹ while that of B_{1g} from 350 to 370 cm⁻¹.^{17,18} In addition, Raman spectroscopy has been considered as a powerful and nondestructive tool to investigate the structural orientation. The grain orientation with respect to the direction and polarization of the incident and scattered light can be reflected by the Raman spectrum according to the Raman selection rule. In this respect, it is unambiguous that Raman spectroscopy is capable of providing strong evidence on the crystallographic information of single crystals or textured films. In view of the above-mentioned facts, the Raman fingerprints of SnO thin films should be addressed to make clear their designation as well as the correlation with the grain orientations.

In the present work, we demonstrate a conversion of (001)-orientated polycrystalline SnO films to (101)-orientated ones on glass, SiO₂/Si and quartz substrates, and then discuss the Raman selection rule in a back scattering mode and the relationship between the Raman spectra and grain orientations of the SnO films, in order to acquire the Raman fingerprints of SnO thin films.

^aDivision of Functional Materials and Nano Devices, Ningbo Institute of Material Technology and Engineering, Chinese Academy of Sciences, Ningbo 315201, People's Republic of China. E-mail: lly@nimte.ac.cn; h_cao@nimte.ac.cn

^bFaculty of Materials Science and Chemical Engineering, Ningbo University, Ningbo 315211, People's Republic of China

Experimental section

SnO thin films with and without Al₂O₃ capping layers were deposited on glass, SiO₂ (110 nm)/Si or quartz substrates by an e-beam evaporation technique. After evacuating to a base pressure of 6.0×10^{-4} Pa, amorphous SnO thin films were evaporated from a high-purity SnO₂ source with a deposition rate of 1.8 nm min^{-1} at room temperature (the growth mechanism was reported elsewhere²⁰). The SnO film thickness was about 30 nm. Al₂O₃ thin films were immediately deposited as the capping layers on the as-deposited SnO films by the same e-beam evaporation system. The Al₂O₃ thickness ($t_{\text{Al}_2\text{O}_3}$) was varied from 0 to 6 nm. The as-deposited SnO films were determined to be amorphous²⁰ and were subjected to undergo rapid thermal annealing (RTA) at 400 °C for 10 min in an ambient Ar atmosphere. The phase composition of the films was characterized in θ - 2θ scans with a multipurpose X-ray diffractometer (Bruker, D8 Advance) working with Cu-K α radiation. The chemical composition was examined by X-ray photoelectron spectroscopy (XPS, Kratos Analytical Ltd, UK) using Al-K α radiation. The Raman spectra of the films were measured using a confocal microscope Raman spectrometer (Renishaw inVia-Reflex) with 180° back scattering geometry. Non-polarized incident light was employed using a 532 nm excitation line created by a second harmonic generation element from a line of 1064 nm generated by Nd:YAG laser. The focused spot size was about 1 μm in diameter.

Results and discussion

Fig. 1a presents XRD patterns of SnO thin films on a glass substrate with different $t_{\text{Al}_2\text{O}_3}$. The bare SnO film exhibits a strong preferred (001) orientation, with a (001) peak located at $\sim 18.4^\circ$ and a (002) peak at $\sim 37.3^\circ$, respectively. With increasing $t_{\text{Al}_2\text{O}_3}$, a (101) peak at $\sim 30.0^\circ$ is present, while the (001) and (002) peaks are suppressed. Especially, the (101) peak is dominant and the (001)-orientated peaks are not observed when $t_{\text{Al}_2\text{O}_3}$ is larger than ~ 5 nm. Similar results are also demonstrated on SiO₂/Si or quartz substrates.

In order to quantify the preferred orientation, the relative texture coefficient was calculated using the peak intensities of X-ray diffraction patterns by the following formula:^{21–23}

$$C_i = 100 \times \frac{I_i/I_{0i}}{\sum_{i=1}^N (I_i/I_{0i})}, \quad (1)$$

where I_i and I_{0i} are the XRD intensities of the actual measurement and the corresponding intensities of the standard powder sample in the i crystal orientation, respectively, and N is the number of peaks in the diffraction patterns. The texture coefficients of (001) and (101) orientations (C_{001} and C_{101}) are calculated and depicted in Fig. 1b. As $t_{\text{Al}_2\text{O}_3}$ increases from 0 to 6 nm, C_{001} decreases from 100% to 0, while C_{101} increases from 0 to 100% for the SnO films deposited whether on glass or quartz. Nevertheless, these phenomena are not that prominent for the SnO films deposited on SiO₂/Si substrates since

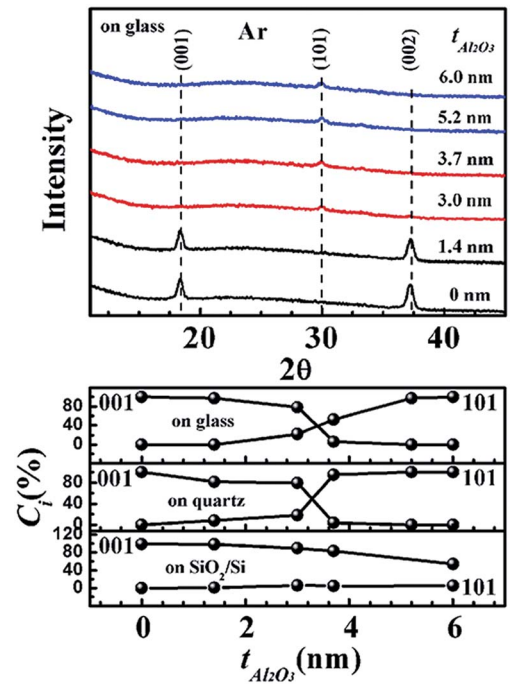


Fig. 1 (a) XRD patterns of Al₂O₃-capped SnO films with varied thickness on a glass substrate. (b) The relative texture coefficient variations as a function of $t_{\text{Al}_2\text{O}_3}$.

additional (110)-orientated grains are present in these films (Fig. 2). What is the reason behind the crystallographic texture conversion?

Generally, grain growth during post-annealing is a coarsening process driven by the strain energy minimization or surface/interface energy minimization.^{24,25} If a film has a different thermal expansion coefficient with the underneath substrate or top-contacted capping layer, differential thermal expansion can lead to a substantial biaxial strain within the film

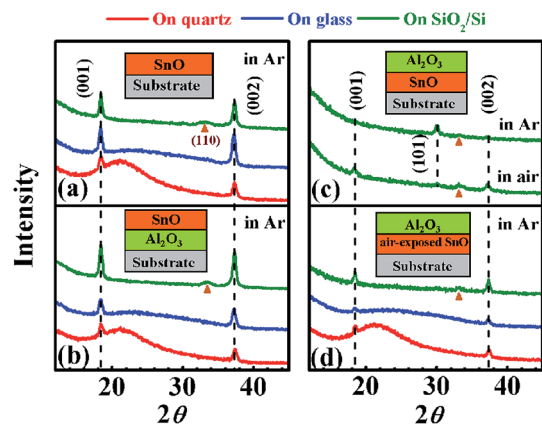


Fig. 2 (a) XRD patterns of bare SnO films on different substrates. (b) XRD patterns of bare SnO films on substrates with an Al₂O₃ inserting layer in between SnO and the substrate. (c) XRD patterns of the SnO films with $t_{\text{Al}_2\text{O}_3} = 6$ nm treated by RTA in an ambient Ar atmosphere and ambient air on a SiO₂/Si substrate, respectively. (d) XRD patterns of the reference SnO films treated by RTA in an ambient Ar atmosphere.

during the heating process. Provided that the film material has elastic anisotropy, this kind of anisotropy does bring about strain energy density differences for diverse grain orientations. That is to say, grains with specific orientations can therefore grow up to minimize the strain. However, the above mechanism is not applicable in our case. As shown in Fig. 2a and b, bare SnO films always favor the (001) preferred orientation on various substrates with different thermal expansion coefficients (glass $\sim 3.25 \times 10^{-6}/\text{K}$, quartz $\sim 0.55 \times 10^{-6}/\text{K}$, Si $\sim 2.59 \times 10^{-6}/\text{K}$ (ref. 26)) or on the substrates with an Al_2O_3 ($5.4 \times 10^{-6}/\text{K}$ (ref. 27)) inserting layer in between the SnO and substrate, implying that the strain induced by the thermal expansion discrepancy has little effect on the SnO grain orientation.

Further more, assuming that the $\text{Al}_2\text{O}_3/\text{SnO}$ interface energy is the primary cause that governs grain orientation evolution, identical XRD results should be observed when the Al_2O_3 layer is located whether on the top surface of the SnO film or underneath it. However, the (001) preferential orientation is observed for the latter case (Fig. 2b), while (101)-orientated growth for the former one (Fig. 1 and 2c). The distinct outcomes indicate that the $\text{Al}_2\text{O}_3/\text{SnO}$ interface energy cannot account for the grain orientation changes.

In particular, the XPS spectra show that the Al_2O_3 -capped films have more metallic Sn than the bare one. Fig. 3a illustrates the core-level spectra of Sn 3d. For the Al_2O_3 -capped films, the Sn 3d spectrum depicts a spin-orbit doublet peak located at ~ 485.9 eV ($\text{Sn}^{2+} 3d_{5/2}$) and ~ 494.3 eV ($\text{Sn}^{2+} 3d_{3/2}$) with two shoulders centered at ~ 484.4 eV ($\text{Sn}^0 3d_{5/2}$) and ~ 492.8 eV ($\text{Sn}^0 3d_{3/2}$). However, only the spin-orbit doublet peak located at ~ 485.9 eV ($\text{Sn}^{2+} 3d_{5/2}$) and ~ 494.3 eV ($\text{Sn}^{2+} 3d_{3/2}$) is observed for the uncapped films. There are three possible origins related to the Sn^0 , *i.e.*, Sn interstitials (Sn_i), oxygen vacancies (V_{O}) or Sn clusters within the SnO. Theoretical calculations proved that

the formation energy is too high (3 eV) to form Sn_i .^{11,28} And no peak assigned to V_{O} can be observed in the Sn-rich film, since the shape and position of the O 1s peak for the bare and Al_2O_3 -capped films are identical, as shown in Fig. 3b. Consequently, it is suggested that the metallic Sn element ($\text{Sn}^0/\text{Sn}^{2+} \sim 6\%$) in the SnO film is in the form of a metal cluster. However, the Sn cluster size is too small to be observed experimentally by XRD measurement, since the Sn cluster is hard to grow up due to a relatively high melting point of up to 600°C .²⁹ Thus, it is believed that the chemical content has a big effect on the preferential growth of SnO thin films. Specifically, metallic Sn-rich and oxygen-rich SnO polycrystalline films favor (101) and (001) preferential orientations, respectively. This suggestion is confirmed again by the result that the SnO film with a 6 nm Al_2O_3 capping layer shows clear (001) and (002) XRD peaks after treatment in air (shown in Fig. 2c). After all, oxygen in air can diffuse into the SnO film through the 6 nm Al_2O_3 thin film (oxygen diffusion coefficient in Al_2O_3 : $5 \times 10^{-25} \text{ cm}^2 \text{ s}^{-1}$)³⁰ and oxidize the residual metallic Sn to some extent during annealing in air. Moreover, it is considered that amorphous (before annealing) SnO films without the capping layer can easily adsorb oxygen when they are exposed in the air. The oxygen adsorption behavior would be prohibited by introducing the Al_2O_3 capping layer onto the SnO surface before it is exposed in the air. In order to gain a more comprehensive understanding, another group of SnO films with a 6 nm-thick Al_2O_3 capping layer were also deposited on different substrates as the reference. The growth conditions were the same as the above-mentioned Al_2O_3 -capped films except that the as-deposited SnO films were taken out of the vacuum chamber and kept in air for 30 h before introducing the Al_2O_3 capping layer. As shown in Fig. 2d, all the reference films display the (001) preferential orientation, in sharp contrast to the (101)-textured growth of the 6 nm- Al_2O_3 -capped SnO films in Fig. 1a. The comparative results indicate that the immediate capping with Al_2O_3 layers can modify the stoichiometry of the SnO films by preventing the oxygen adsorption behavior, resulting in the grain growth orientation conversion. However, the adsorbed oxygen is unable to oxidize all the residual metallic Sn in thick SnO films (>30 nm). Hence, thick bare SnO films present a (101) XRD peak, as seen that this peak intensity increases with the film thickness (ESI, Fig. S1†). Nevertheless, the (001)-orientated peaks of the thick films can also be suppressed by immediately capping Al_2O_3 layers (ESI, Fig. S2†), again verifying the effect of the Al_2O_3 capping layer. Anyway, all the above results illustrate that it is the chemical composition, rather than the film strain or interface energy between Al_2O_3 and SnO that governs the orientation conversion. However, the reason why the grain orientation depends on the chemical composition is unclear now and needs further investigation.

The control of SnO grain orientation facilitates describing the relationship between the Raman spectrum fingerprint and the grain orientation. Fig. 4a displays the Raman spectra of SnO films with different $t_{\text{Al}_2\text{O}_3}$. To simplify, the wavenumber range of $80\text{--}240 \text{ cm}^{-1}$ was picked out. The Raman spectrum of the bare SnO film shows only one peak located at 210 cm^{-1} . With increasing $t_{\text{Al}_2\text{O}_3}$, the 110 cm^{-1} peak intensity increases

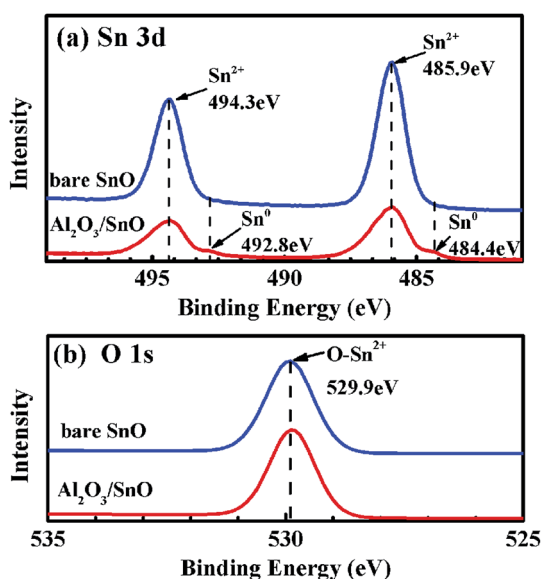


Fig. 3 (a) XPS spectra of Sn 3d for the bare SnO and Al_2O_3 -capped SnO films followed by annealing in Ar, respectively. (b) XPS spectra of O 1s for the bare SnO and Al_2O_3 -capped SnO films, respectively.

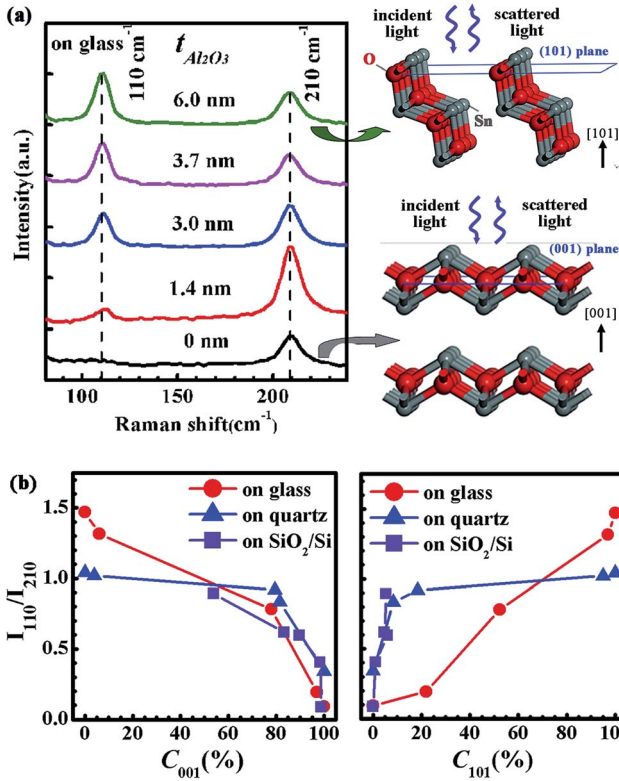


Fig. 4 (a) Raman spectra of Al_2O_3 -capped SnO films with varied thickness on a glass substrate. (b) The I_{110}/I_{210} ratio variations as a function of C_{001} and C_{101} , respectively.

gradually, *e.g.*, the 110 cm^{-1} peak intensity is even more intensive than that of the 210 cm^{-1} peak when $t_{\text{Al}_2\text{O}_3}$ is 6 nm. It is noteworthy that the dependence of the 110 cm^{-1} Raman peak intensity on $t_{\text{Al}_2\text{O}_3}$ is the same as C_{101} but opposite to C_{001} . Furthermore, the I_{110}/I_{210} ratio (I_{110} and I_{210} are the intensities of the 110 cm^{-1} and 210 cm^{-1} Raman peaks, respectively) is

plotted as a function of the relative texture coefficients (C_{001} and C_{101}) in Fig. 4b. The I_{110}/I_{210} ratio increases with C_{101} but decreases with C_{001} , irrespective of the substrates used. And it is also demonstrated that the 110 cm^{-1} peak intensity increases with the SnO film thickness (ESI, Fig. S3†), in accordance with the increasing intensity of the (101) grains detected by XRD. These results imply that the Raman fingerprint is tightly coupled with the grain growth orientation. Moreover, their correlation could be clarified theoretically through the Raman selection rule.

According to the scattering intensity formula, the intensity of Raman scattered light is directly proportional to the Raman scattering efficiency:

$$S = \left| e_i \frac{d\alpha}{d\xi} e_s \right|^2. \quad (2)$$

Here e_i and e_s are the polarization direction of the incident light and scattered light, respectively, $\frac{d\alpha}{d\xi}$ the first-order derivative of polarizability (also called the Raman tensor that can be written in a matrix form, as shown in Table 1). Therefore, the corresponding Raman spectrum can be observed experimentally on the condition that S is not equal to zero.

Considering the back scattering geometry that the incident and scattered lights both propagate perpendicular to the film surface and the e_i and e_s are parallel to each other, the values of S corresponding to the A_{1g} , B_{1g} and E_g vibration modes are respectively derived for SnO with different orientations, as displayed in Table 1. It can be definitely found out that the Raman scattering efficiency of low-frequency E_g mode is zero for the (001) plane orientation and maximum for the (101) orientation, which agrees well with our observations (Fig. 4). In contrast, the Raman scattering efficiency of B_{1g} mode for the (001) plane orientation is larger than that for the (101) orientation. These results undoubtedly manifest that the 110 cm^{-1} Raman peak

Table 1 The Raman scattering efficiency (S) for different modes of SnO with different grain orientations. Assume that the Raman scattering is in back scattering mode with polarized and non-polarized incident lights, respectively^a

Modes	S				
Active Tensor	Orientation e_i, e_s	001 ($\cos \theta, \sin \theta, 0$)	101 ($\sin \varphi \cos \alpha, \cos \varphi, -\sin \varphi \sin \alpha$)	110 ($\frac{\sqrt{2}}{2} \sin \phi, -\frac{\sqrt{2}}{2} \sin \phi, \cos \phi$)	100 ($0, \cos \beta, \sin \beta$)
A_{1g} $\begin{pmatrix} a & 0 & 0 \\ 0 & a & 0 \\ 0 & 0 & b \end{pmatrix}$	Polarized	a^2	$ a + (b - a)\sin^2 \alpha \sin^2 \varphi ^2$	$ a \sin^2 \phi + b \cos^2 \phi ^2$	$ a \cos^2 \beta + b \sin^2 \beta ^2$
	Non-polarized	a^2	$a^2 + 0.618a(b - a) + \frac{1}{7}(a - b)^2$	$\frac{3}{8}a^2 + \frac{3}{8}b^2 + \frac{1}{4}ab$	$\frac{3}{8}a^2 + \frac{3}{8}b^2 + \frac{1}{4}ab$
B_{1g} $\begin{pmatrix} c & 0 & 0 \\ 0 & -c & 0 \\ 0 & 0 & 0 \end{pmatrix}$	Polarized	$c^2[1 - 2 \sin^2 \theta]^2$	$ c \sin^2 \varphi (1 + \cos^2 \alpha) - c ^2$	0	$c^2 \cos^4 \beta$
	Non-polarized	$\frac{1}{2}c^2$	$\frac{1}{3}c^2$	0	$\frac{3}{8}c^2$
E_g $\begin{pmatrix} 0 & 0 & d \\ 0 & 0 & 0 \\ d & 0 & 0 \end{pmatrix}$	Polarized	0	$d^2 \sin^4 \varphi \sin^2 2\alpha + d^2 \sin^2 \alpha \sin^2 2\varphi$	$d^2 \sin^2 2\phi$	$d^2 \sin^2 2\beta$
	Non-polarized	0	$\frac{2}{3}d^2$	$\frac{1}{2}d^2$	$\frac{1}{2}d^2$

^a Assume that the [001] direction is defined as the z axis. α is the angle between the x axis and (101) plane. θ, φ, ϕ and β are the angles between e_i and the x axis in the (001) plane, y axis in the (101) plane, z axis in the (110) plane and y axis in the (100) plane, respectively.

should be assigned to the E_g mode. In addition, the Raman characteristic peaks as well as the I_{110}/I_{210} ratio in the Raman peak of polycrystalline SnO films, as a unique fingerprint, are capable of reflecting grain growth and texture evolution.

Conclusions

SnO (001)- or (101)-textured films were respectively fabricated and the conversion between these two orientations was also demonstrated. The preferred orientation conversion was tuned by modifying the stoichiometry of SnO films by introducing an Al_2O_3 capping layer. It was presented that O-rich and Sn-rich SnO films favor (001) and (101) preferred orientations, respectively. Moreover, it was confirmed that the 110 cm^{-1} Raman peak should be assigned to the E_g mode of SnO. The I_{110}/I_{210} ratio in the Raman peak increased with a texture coefficient of (101) but decreased with a texture coefficient of (001), irrespective of the substrates used, indicating that the Raman fingerprints of polycrystalline SnO films can reflect texture growth and allow us to identify the grain orientations.

Acknowledgements

This work is supported by the National Natural Science Foundation of China (Grant no. 11104289), the Chinese National Program on Key Basic Research Project (2012CB933003), and the Science and Technology Innovative Research Team of Ningbo Municipality (2009B21005).

Notes and references

- 1 J. Ning, T. Jiang, K. Men, Q. Dai, D. Li, Y. Wei, B. Liu, G. Chen, B. Zou and G. Zou, *J. Phys. Chem. C*, 2009, **113**, 14140.
- 2 J. Ning, Q. Dai, T. Jiang, K. Men, D. Liu, N. Xiao, C. Li, D. Li, B. Liu, B. Zou, G. Zou and W. W. Yu, *Langmuir*, 2009, **25**, 1818.
- 3 S. Filippov, X. J. Wang, M. Devika, N. Koteeswara Reddy, C. W. Tu, W. M. Chen and I. A. Buyanova, *J. Appl. Phys.*, 2013, **113**, 214302.
- 4 E. Fortunato, P. Barquinha and R. Martins, *Adv. Mater.*, 2012, **24**, 2945.
- 5 J. A. Caraveo-Frescas, P. K. Nayak, H. A. Al-Jawhari, D. B. Granato, U. Schwingenschlöggl and H. N. Alshareef, *ACS Nano*, 2013, **7**, 5160.
- 6 L. Y. Liang, Z. M. Liu, H. T. Cao, Z. Yu, Y. Y. Shi, A. H. Chen, H. Z. Zhang, Y. Q. Fang and X. L. Sun, *J. Electrochem. Soc.*, 2010, **157**, H598.
- 7 k. Nomura, T. Kamiya and H. Hosono, *Adv. Mater.*, 2011, **23**, 343.
- 8 J. A. Caraveo and H. N. Alshareef, *Appl. Phys. Lett.*, 2013, **103**, 222103.
- 9 L. Y. Liang, H. T. Cao, X. B. Chen, Z. M. Liu, F. Zhuge, H. Luo, J. Li, Y. C. Lu and W. Lu, *Appl. Phys. Lett.*, 2012, **100**, 263502.
- 10 Y. Duan, *Phys. Rev. B: Condens. Matter Mater. Phys.*, 2008, **77**, 045332.
- 11 A. Togo, F. Oba, I. Tanaka and K. Tatsumi, *Phys. Rev. B: Condens. Matter Mater. Phys.*, 2006, **74**, 195128.
- 12 W. Guo, L. Fu, Y. Zhang, K. Zhang, L. Y. Liang, Z. M. Liu, H. T. Cao and X. Q. Pan, *Appl. Phys. Lett.*, 2010, **96**, 042113.
- 13 V. Krasevec and Z. Skraba, *Thin Solid Films*, 1985, **129**, L61.
- 14 Y. Ogo, H. Hiramatsu, K. Nomura, H. Yanagi, T. Kamiya, M. Hirano and H. Hosono, *Appl. Phys. Lett.*, 2008, **93**, 032113.
- 15 J. Geurts, S. Rau, W. Richter and F. J. Schmitte, *Thin Solid Films*, 1984, **121**, 217.
- 16 M. K. Hota, J. A. Caraveo-Frescas, M. A. McLachlan and H. N. Alshareef, *Appl. Phys. Lett.*, 2014, **104**, 152104.
- 17 E. L. Peltzer y Blanca, A. Svane, N. E. Christensen, C. O. Rodriguez, O. M. Cappannini and M. S. Moreno, *Phys. Rev. B: Condens. Matter Mater. Phys.*, 1993, **48**, 15712.
- 18 S. Koval, R. Burriel, M. G. Stachiotti, M. Castro, R. L. Migoni, M. S. Moreno, A. Varela and C. O. Rodriguez, *Phys. Rev. B: Condens. Matter Mater. Phys.*, 1999, **60**, 14496.
- 19 H. Luo, L. Y. Liang, H. T. Cao, Z. M. Liu and F. Zhuge, *ACS Appl. Mater. Interfaces*, 2012, **4**, 5673.
- 20 L. Y. Liang, Z. M. Liu, H. T. Cao and X. Q. Pan, *ACS Appl. Mater. Interfaces*, 2010, **2**, 1060.
- 21 A. M. Rashidi, M. Hayati and A. Rezaei, *Solid State Sci.*, 2011, **13**, 1589.
- 22 E. A. Pavlatou, M. Raptakis and N. Spyrellis, *Surf. Coat. Technol.*, 2007, **201**, 4571.
- 23 S.-H. Kim, H.-J. Sohn, Y.-C. Joo, Y.-W. Kim, T.-H. Yim, H.-Y. Lee and T. Kang, *Surf. Coat. Technol.*, 2005, **199**, 43.
- 24 C. V. Thompson, *Interface Sci.*, 1998, **6**, 85.
- 25 C. V. Thompson and R. Carel, *J. Mater. Sci. Eng. B*, 1995, **32**, 211.
- 26 Y. Okada and Y. Tokumaru, *J. Appl. Phys.*, 1984, **56**, 314.
- 27 M. G. Beghi and L. Luzzi, *Rev. Sci. Instrum.*, 2000, **71**, 154.
- 28 J. P. Allen, D. O. Scanlon, L. F. J. Piper and G. W. Watson, *J. Mater. Chem. C*, 2013, **1**, 8194.
- 29 A. A. Shvartsburg and M. F. Jarrold, *Phys. Rev. Lett.*, 2000, **85**, 2530.
- 30 L. Y. Liang, Z. M. Liu, H. T. Cao, Y. Y. Shi, X. L. Sun, Z. Yu, A. H. Chen, H. Z. Zhang and Y. Q. Fang, *ACS Appl. Mater. Interfaces*, 2010, **2**, 1565.